NOVEL FRACTIONAL MODELING BASED ON CATTANEO HEAT FLUX FOR ENHANCING THERMAL PERFORMANCE OF U-TUBE PARABOLIC TROUGH COLLECTORS

Mohamed R. Abdo [a, *], Manal E. Ali [a], Swellam W. Sharshir [b], I. L. El-Kalla [c]

[a] *Department of Physics and Engineering Mathematics, Faculty of Engineering, Kafrelsheikh University, Kafrelsheikh 33516, Egypt*

[b] *Mechanical Engineering Department, Faculty of Engineering, Kafrelsheikh University, Kafrelsheikh 33516, Egypt*

[c] *Mathematics and Engineering Physics Department, Engineering Faculty, Mansoura University, Mansoura 35516, Egypt,*

[*] Corresponding author: M. R. Abdo (mohamad_reda@eng.kfs.edu.eg)

ABSTRACT. This paper presents a new approach for modeling U-type parabolic trough collectors (PTCs). The model incorporates a concept called "time-fractional single-phase-lag" and accounts for thermal wave effects within the collector. Researchers first optimized the model using experimental data from Kafrelsheikh, Egypt, to achieve the most accurate predictions. Optimum solution obtained was for the case of fractional Fourier model, where $\beta = 0.8$, and $\tau = 0$, at which calculated average water outlet temperature was $50.872\,°C$ compared with an average value of $50.885\,°C$ obtained from experimental results. The most significant performance improvements were achieved by coating the absorber tube with black paint containing nanoparticles. Here, the best results were obtained with a 5% mass concentration of carbon nanotubes (CNTs) in the paint. This configuration led to a substantial increase in the average water temperature difference between the outlet and inlet ($21.7\,°C$) and a significant improvement in overall thermal efficiency (33.67%).

1. INTRODUCTION

Driven by concerns about running out of fossil fuels and the threat of global warming, researchers are now focusing on clean and sustainable energy sources. Their studies have shown that renewable energy is the most promising solution for the future because it doesn't produce greenhouse gases and is constantly available. Among all renewable resources, solar energy is the most widely used globally, offering a variety of solutions across different applications. It plays a vital role in industrial processes by providing both hot water and electricity[1]. Regions with strong sunlight are ideal for this technology. In these regions, concentrating solar collectors can trap a significant amount of sunlight, achieving impressive temperatures above 400 °C and transforming that energy into usable heat with outstanding efficiency [2,3]. Hence, solar energy technologies are becoming increasingly attractive and practical for a wide range

of applications, including heating, cooling, chemical processes, desalination and even hydrogen synthesis[4]. Recognizing the immense potential of solar energy, researchers have prioritized optimizing its capture and utilization across a wide range of applications.

The key to a successful solar system is capturing sunlight efficiently. Different collector technologies, like PTCs, flat plates, and parabolic dishes, address diverse needs [5–9]. On the other hand, flat plate collectors excel in heating fluids like air, water, or water-antifreeze mixtures. Their primary objective is to maximize solar energy capture while maintaining cost-effectiveness. Finally, parabolic dish collectors are often paired with parabolic dish engines, which function as electric generators without relying on fossil fuels like oil or coal.[10].

Parabolic trough collectors (PTCs) dominate the field of solar concentration, accounting for a staggering 90% of all concentrating solar power

systems in operation [11]. Their design is ingenious: they use reflective surfaces to focus sunlight onto an absorber tube encased in a vacuum, effectively heating a working fluid within. This technology holds immense potential for various industries due to its ability to efficiently generate medium to high-temperature heat (100°C to 300°C) in the form of steam or hot water[12–15]. Applications span a wide range, including food processing, beverage production, textiles, chemicals, laundry, and more – all sectors requiring such thermal energy[14]. This promising outlook has fueled extensive research efforts, with many studies exploring innovative PTC designs and optimizing existing collector performance[16].

Researchers explore modifications to boost the thermal performance of PTCs [17–22]. Passive modifications focus on enhancing heat transfer fluids thermophysical properties which can be achieved by using nanofluids. Nanofluids are fluids that incorporate nanoscale particles, typically metal oxides, which can significantly improve properties like thermal conductivity and heat capacity [23]. Nanoparticles also alter the fluid's viscosity and density, further influencing heat transfer. Researchers have found that the addition of nanoparticles enhances the base fluid's thermal properties due to their high and unique radiative and volume-to-surface ratio. For nanofluid production, commonly used nanoparticles are Al, Au, Cu, Ni, Fe, CuO, Al_2O_3, ZnO, TiO_2, SiO_2, and Fe_2O_3 which reign supreme as the most commonly employed nanoparticles [24]. For the applications to heat transfer, CuO nanoparticles, often combined with deionized water, are particularly favored [25–27].   Additionally, using CuO nanoparticles in deionized water creates a highly efficient HTF. Studies confirm that CuO nanofluids can lead to substantial improvements in PTC thermal efficiency [28] .

To optimize the design and performance of parabolic trough power plants, it's crucial to carefully analyze heat losses during the initial planning stages. This analysis helps determine the ideal size of the plant and assess how factors like absorber pipe deterioration and flow rate of HTF can affect the overall system. Forristal's work stands out for creating a detailed one-dimensional model to analyze heat transfer in a parabolic trough collector's receiver element, enabling PTC performance calculations.[29]. He developed a comprehensive 1D heat transfer model for PTC heat receiver elements, used extensively for performance calculation and validation. He also compared the efficacy of 1D and 2D models under various conditions. Huang et al. [30] developed an analytical model to precisely calculate the optical efficiency of a PTC with evacuated tube receiver, which is capable of optimizing solar irradiation distribution and incorporating factors like

optical and tracking errors, position errors, and material properties to simulate PTC performance accurately. Patil et al. [31] used numerical simulations to analyze thermal losses in a non-evacuated receiver tube. They considered various factors influencing heat loss, including the uneven distribution of solar radiation on the tube surface, the gap between the absorber and the glass envelope (annulus distance), and the sun's position in the sky (hour angle). Their objective was optimizing this non-evacuated receiver design using computational fluid dynamics (CFD) to minimize thermal losses. In their work, Amal and Francisco [32] employed a numerical approach to investigate the behavior of a PTC using a HTF with thermophysical properties changes with temperature.

Fractional calculus, a field of mathematics gaining significant traction in recent years, has demonstrated its effectiveness in various applications. From signal processing and control engineering to communication, image processing, and even scientific disciplines like heat transfer, biology, and chemistry, fractional calculus is proving its versatility [33–40]. Several definitions of fractional derivatives exist, including Riemann-Liouville, Caputo, Atangana-Baleanu, and Caputo-Fabrizio [41–43]. Additionally, Khalil introduced the Conformable fractional derivative, offering a definition that aligns well with the concept of the ordinary derivative [44]. This growing interest and diverse applications highlight the potential of fractional calculus in various scientific and engineering fields. Research in fractional-reaction-diffusion equations, which involve both constant and distributed order derivatives, has been extensive. Numerous studies have explored analytical and numerical techniques to solve these nonlinear and unsteady equations[45–49]. For instance, Zhang and Wei [50] studied fractional-order models for supercapacitors in electric vehicles, they compared their results with experimental data achieving only 2% fitting accuracy. El-Gazar et al. [40] developed a fractional model for a conventional solar still using hybrid nanofluid, they compared their results with experimental data achieving only 1.486% relative error for summer conditions.

For the past two centuries, Fourier's Law has been the cornerstone of heat transfer analysis[51]. However, it struggles to accurately predict system behavior at extremely small scales (both in terms of space and time). This limitation manifests as the "heat conduction paradox" (HCP), as Fourier's Law fails to capture the initial, rapid changes in temperature distribution [52]. Limitations in the classical Fourier law for accurately predicting temperature have driven the development of numerous non-Fourier models. These models aim to provide a more comprehensive understanding of heat transfer phenomena and their applications in real-world systems. One prominent example is the Cattaneo

model, proposed in recent decades. This model addresses the shortcomings of the Fourier law by incorporating the concept of lagging time (τ) which accounts for the time delay between changes in temperature and the resulting heat flux. Due to its ability to capture this crucial aspect of heat transfer, engineers and scientists pay great attention to the Cattaneo model. For instance, Milad et al. [53] studied anomalous heat conduction in absorber plate of a solar collector using time-fractional single-phase-lag model. In another example, Zahra et al. successfully modeled the laser drilling process using a new fractional model and a meshless method, achieving excellent agreement with experimental data [54]. These examples showcase the growing body of research applying fractional calculus to model complex phenomena in various fields.

Despite considerable research on predicting and enhancing PTC performance, the quest for a flawless prediction model remains elusive. Existing models, often based on the classical Fourier law, show significant discrepancies between theoretical results and real-world experiments. This paper proposes a novel time-fractional single-phase-lag model for U-tube PTCs aimed at achieving more accurate results with minimal errors compared to experimental data. The approach entails constructing and solving the new fractional model for various relaxation times and fractional orders. The resulting data will be plotted and compared with experimental data to identify the configuration with the lowest error. Next, we will investigate the impact of introducing different nanomaterials (CuO, TiO$_2$, and Al$_2$O$_3$) at varying volume concentrations (both individually and in mixtures) into the heat transfer fluid (HTF) using the optimal model configuration. Finally, we will explore the effect of coating the PTC absorber tube with black paint mixed with different mass concentrations of carbon nanotubes (CNTs) and CuO nanoparticles (both individually and in mixtures). This approach aims to improve solar absorptance and consequently enhance the overall thermal performance of the PTC system.

2. MATHEMATICAL MODEL

In this section a new mathematical model based on Cattaneo heat flux for a conventional PTC composed of four main parts including a parabolic mirror, absorber U-tube shaped inserted into a glass evacuated receiver tube and the main structure supporting the previous components, as shown in Fig. 1 and Fig. 2. Dimensions used for modeling will be the same used for fabricating PTC build by Hamada et al. [55] for testing the accuracy of the new modeling method, these dimensions are mentioned in Table 1.

The new model can be divided into three main control volumes, which are the heat transfer fluid (HTF), the absorber tube and the glass receiver tube. For convenience, the U-type absorber of 3.6 m unfolded length with inlet and outlet located at one side will be treated as unfolded tube of the same length inserted into evacuated tube opened at both ends where absorber tube inlet is located at one of its ends while its outlet is located at the other end, therefore, the length of the evacuated tube and the parabolic mirror will be assumed to be 3.6 m which is the unfolded absorber U-tube length, whereas parabolic mirror width will be reduced to half of its original value to be 0.9 m to maintain the same amount of received incident solar radiation on entire PTC surface.
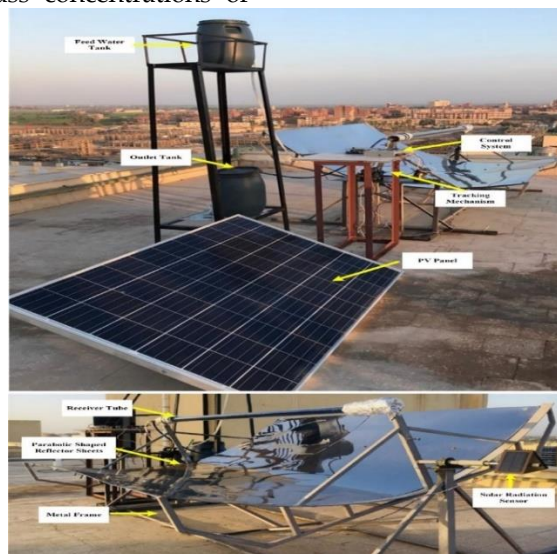

Fig. 1. Photograph of the reference experimental setup [55]

Fig. 2. (a) schematic of the reference apparatus [55], (b) inner details of the evacuated tube.

Table 1. Dimensions of reference PTC[55]

Variable	Quantity	Unit
Concentration ratio	18.5	-
Reflecting mirror length	1.8	Meter
Width of the aperture	1.8	Meter
Focal length	0.6	Meter
Evacuated tube length	1.8	Meter
d_{r-in}	48	Millimeter
d_{r-o}	50	Millimeter
d_{abs-in}	9	Millimeter
d_{abs-o}	15	Millimeter
Absorber tube unfolded length	3.6	Meter

2.1. CONVENTIONAL U-TUBE PTC FRACTIONAL SINGLE PHASE LAG MODEL

According to Cattaneo[56], conduction heat transfer equation is modified to take the form of:

$$q(x, t + \tau) = -kA_c \frac{\partial T(x,t)}{\partial x} \tag{1}$$

where q indicates conduction heat flux, and $\tau \left(= \frac{\alpha}{c^2}\right)$ represents "relaxation time", which is the time lag required to create steady heat conduction in a volume element once establishing a temperature gradient across it [57]. Interestingly, Eq. (2) simplifies to the classical Fourier heat conduction equation when the speed of energy transfer approaches infinity ($c \to \infty$).

Taking the first-order fractional Taylor series expansion [58] of Eq.(1), we get:

$$q(x, t + \tau) = q(x, t) + \frac{\tau^\alpha}{\Gamma(1 + \alpha)} \frac{\partial^\alpha q(x,t)}{\partial t^\alpha} \tag{2}$$
$$= -kA_c \frac{\partial T(x,t)}{\partial x}$$

where $\frac{\partial^\alpha}{\partial t^\alpha}$ is the Caputo fractional derivative, and $0 < \alpha < 1$. Interestingly, for the case of $\alpha = 1$, Eq. (2) turns into classical Taylor series.

Fig. 3. Energy balance for (a) HTF control volume, (b) Absorber tube control volume, (c)Receiver tube control volume.

2.1.1. Heat Transfer Fluid

As regards Fig. 3 (a), the energy balance equation for HTF element results in:

$$-\rho_f u_f A_{cf} c_{pf} \frac{\partial T_f(x,t)}{\partial x}\Delta x - \frac{\partial q_f(x,t)}{\partial x}\Delta x \tag{3}$$
$$+ h_{con,f-abs}\pi\bar{d}_{abs}\Delta x\big(T_{abs}(x,t)$$
$$- T_f(x,t)\big) = \rho_f A_{cf} c_{pf}\frac{\partial T_f(x,t)}{\partial t}\Delta x$$

Dividing by Δx and evaluating the limit as $\Delta x \to 0$ yields:

$$-\rho_f u_f A_{cf} c_{pf}\frac{\partial T_f(x,t)}{\partial x} - \frac{\partial q_f(x,t)}{\partial x} \tag{4}$$
$$+ h_{con,f-abs}\pi\bar{d}_{abs}\big(T_{abs}(x,t)$$
$$- T_f(x,t)\big) = \rho_f A_{cf} c_{pf}\frac{\partial T_f(x,t)}{\partial t}$$

Using Eq.(2), the governing heat balance equation for the fluid element becomes:

$$h_{con,f-abs}\pi\bar{d}_{abs}\big(T_{abs} - T_f\big) - \rho_f u_f A_{cf} c_{pf}\frac{\partial T_f}{\partial x} + k_f A_{cf}\frac{\partial^2 T_f}{\partial x^2} \tag{5}$$
$$= \rho_f A_{cf} c_{pf}\left(\frac{\partial T_f}{\partial t} + \frac{\tau_f}{\Gamma(1+\alpha)}\frac{\partial^{1+\alpha}T_f}{\partial t^{1+\alpha}}\right)$$

For complete time-fractional model; the time partial derivative term $\left(\frac{\partial T_f}{\partial t}\right)$ is modified into the fractional form $\left(\frac{\partial^\beta T_f}{\partial t^\beta}\right)$, where $0 < \beta < 1$; in order to study the effect of altering the order of all time-derivative terms. Therefore, Eq.(5) can be written as follows:

$$h_{con,f-abs}\pi\bar{d}_{abs}\big(T_{abs} - T_f\big) - \rho_f u_f A_{cf} c_{pf}\frac{\partial T_f}{\partial x} + k_f A_{cf}\frac{\partial^2 T_f}{\partial x^2} \tag{6}$$
$$= \rho_f A_{cf} c_{pf}\left(\frac{\partial^\beta T_f}{\partial t^\beta} + \frac{\tau_f}{\Gamma(1+\alpha)}\frac{\partial^{1+\alpha}T_f}{\partial t^{1+\alpha}}\right),$$
$$0 < \beta < 1 \text{ and } 0 < \alpha < 1$$

where τ_f represents HTF relaxation time, while ρ_f, c_{pf} and k_f represent HTF density (kg/m^3), specific heat $(J/kg°C)$ and thermal conductivity $(W/m°k)$ respectively, T_f and T_{abs} represent temperature of the HTF and the absorber tube measured in (K) respectively, A_{cf} is the HTF cross-sectional area (m^2), $\bar{d}_{abs}$ is the mean diameter of the absorber tube (m) and u_f represents HTF mean velocity (m/s).

Also, $h_{con,f-abs}$ represents convection heat transfer coefficient between the absorber and the HTF measured in $(W/m^2°k)$, and can be calculated by [59], as follows:

$$h_{con,f-abs} = \frac{Nu\, k_f}{d_{abs-in}} \tag{7}$$

where Nu represents HTF Nusselt number.

2.1.2. Absorber tube
As regards Fig. 3 (b), the energy balance equation for absorber tube element results in:

$$I_{abs}(t)W\Delta x - \frac{\partial q_{abs}(x,t)}{\partial x}\Delta x - h_{con,f-abs}\pi\bar{d}_{abs}\Delta x\left(T_{abs}(x,t) - T_f(x,t)\right) \tag{8}$$
$$- h_{con,abs-r}\pi\bar{d}_{abs}\Delta x\big(T_{abs}(x,t) - T_r(x,t)\big)$$
$$- h_{rad,abs-r}\pi\bar{d}_{abs}\Delta x\big(T_{abs}^4(x,t) - T_r^4(x,t)\big)$$
$$= \rho_{abs}A_{c-abs}c_{p-abs}\frac{\partial T_{abs}(x,t)}{\partial t}\Delta x$$

where W is the aperture width (m), ρ_{abs}, c_{p-abs} and k_{abs} represent absorber tube density (kg/m^3), specific heat $(J/kg°C)$ and thermal conductivity $(W/m°k)$ respectively, T_r represents temperature of the receiver measured in (K),

$h_{con,abs-r}$ represents natural convection heat transfer coefficient for air involved by the absorber and receiver tubes, which can be calculated as follows [59]:

$$h_{con,abs-r} = \frac{2k_{eff}}{ln(d_{r-in}/d_{abs-o})\cdot d_{abs-o}} \tag{9}$$

where

$$\frac{k_{eff}}{k_{anu}} = 0.386\left(\frac{Pr_{anu}}{0.861 + Pr_{anu}}\right)^{1/4}(Ra_c)^{1/4} \tag{10}$$

where k_{anu} and Pr_{anu} represent the thermal conductivity $(W/m°C)$ and the Prandtl number for the air in the annulus and these properties have been determined at (T_{av}).

$$T_{av} = \frac{T_{abs} + T_r}{2},$$

while Ra_c represent the Rayleigh number in the annulus, which should be determined at (L_c).

$$L_c = \frac{2[ln(d_{r-in}/d_{abs-o})]^{4/3}}{[(d_{r-in})^{-3/5} + (d_{a-o})^{-3/5}]^{5/3}},$$

these equations are valid for: $0.7 \le Pr \le 6000$, and $Ra_c \le 10^7$[59].

$h_{rad,abs-r}$ represents radiation heat transfer coefficient, due to surface-to-surface radiative heat transfer between the absorber and receiver tubes, which can be calculated as follows [59,60]:

$$h_{rad,abs-r} = \frac{\sigma}{\frac{1}{\varepsilon_{abs}} + \frac{(1-\varepsilon_r)d_{abs-o}}{\varepsilon_r d_{r-in}}}, \tag{13}$$

where ε_{abs} and ε_r represent the emissivity of the absorber and the receiver tubes, respectively, and σ can be considered as the Stephen Boltzmann constant.

I_{abs} represents instantaneous amount of solar energy absorbed by the absorber tube (W/m^2), and can be calculated as follow[61,62]:

$$I_{abs}(t) = \eta_{opt}I(t), \tag{14}$$

where I is the instantaneous solar irradiation (W/m^2), and η_{opt} is the PTC optical efficiency, and can be calculated using this equation[63]:

$$\eta_{opt} = \rho_m \tau_g \alpha_{abs}\gamma \tag{15}$$

where ρ_m, τ_g, α_{abs}, and γ represent the reflectance of the mirror sheets, the transmittance of the glass cover of the receiver tube, the absorbance of the absorber tube, and the intercept factor, which represents the system losses, respectively.

Dividing Eq.(8) by Δx and evaluating the limit as $\Delta x \to 0$, then using Eq.(2), the governing heat balance equation for complete time-fractional model for the absorber tube element becomes:

$$I_{abs}(t)W - h_{f-abs}\pi\bar{d}_{abs}\big(T_{abs} - T_f\big) - h_{con,abs-r}\pi\bar{d}_{abs}\big(T_{abs} - T_r\big) \tag{16}$$
$$- h_{rad,abs-r}\pi\bar{d}_{abs}\big(T_{abs}^4 - T_r^4\big) + k_{abs}A_{c-abs}\frac{\partial^2 T_{abs}}{\partial x^2}$$
$$= \rho_{abs}A_{c-abs}c_{p-abs}\left(\frac{\partial^\beta T_{abs}}{\partial t^\beta} + \frac{\tau_{abs}}{\Gamma(1+\alpha)}\frac{\partial^{1+\alpha}T_{abs}}{\partial t^{1+\alpha}}\right),$$

where $0 < \beta < 1, 0 < \alpha < 1$, and τ_{abs} represents absorber tube relaxation time.

2.1.3. Glass receiver tube

On the same manner for deriving heat balance equation for the absorber tube and the HTF, and by considering Fig. 3 (c), the governing heat balance equation for glass receiver tube element becomes:

$$I_r(t)W + h_{con,abs-r}\pi \bar{d}_{abs}(T_{abs} - T_r)$$
$$+ h_{rad,abs-r}\pi \bar{d}_{abs}(T_{abs}^4 - T_r^4) - h_{con,r-atm}\pi \bar{d}_r(T_r - T_{atm})$$
$$- h_{rad,r-sky}\pi \bar{d}_r(T_r^4 - T_{sky}^4) + k_r A_{c-r}\frac{\partial^2 T_r}{\partial x^2}$$
$$= \rho_r A_{c-r}c_{p-r}\left(\frac{\partial^\beta T_r}{\partial t^\beta} + \frac{\tau_r}{\Gamma(1+\alpha)}\frac{\partial^{1+\alpha}T_r}{\partial t^{1+\alpha}}\right) \quad (17)$$

where $0 < \beta < 1, 0 < \alpha < 1$, and I_r measured in (W) represents the instantaneous tiny amount of absorbed solar energy by the glass receiver tube, which can be determined as follows[61,62]:

$$I_r(t) = \rho_m \alpha_r \gamma I_t(t), \quad (18)$$

where α_r represents the absorptivity of the glass receiver tube.

while $h_{con,r-atm}$ represents the coefficient of the convective heat transfer of the outside air, and the mathematical expression, which can be employed to determine its value is as below [59]:

$$h_{con,r-atm} = \frac{Nu_{atm} \cdot k_{atm}}{d_{r-o}}, \quad (19)$$

where k_{atm} (W/m°C) is the thermal conductivity of the outside air and can be evaluated at (T_m).

$$T_m = \frac{T_r + T_{atm}}{2} \quad (20)$$

while Nu_{atm} represents the Nusselt number of the atmospheric air, and the mathematical expression when there has been wind [59]:

$$Nu_{atm} = C\, Re_{atm}{}^m Pr_{atm}{}^n \left(\frac{Pr_{atm}}{Pr_r}\right)^{1/4} \quad (21)$$

where C and m can be considered as constants and can be extracted from Table 2 ,while n represents a constant, whose value can be:

$$n = 0.37 \quad if\ Pr_{atm} \leq 10 \quad (22)$$

$$n = 0.36 \quad if\ Pr_{atm} \geq 10 \quad (23)$$

all the parameters utilized in Eq. (21) have been determined at (T_{atm}) except Pr_r has been determined at (T_r).

Also, $h_{rad,r-sky}$, represents radiation heat transfer coefficient between receiver glass tube and sky and can be determined by utilizing the following equation [59]:

$$h_{rad,r-sky} = \varepsilon_r \sigma \quad (24)$$

where T_{sky} (°C) can be assumed to be: $T_{sky} = T_{atm} - 8$

Table 2. The values of C and m constants [59]

Re_{atm}	C	m
$1 - 40$	0.75	0.4
$40 - 10^3$	0.51	0.5
$10^3 - 2 \times 10^5$	0.26	0.6
$2 \times 10^5 - 1 \times 10^6$	0.076	0.7

Inserting nanoparticles with specific thermal properties into the HTF, or even coating the receiver tube with paint mixed with them can enhance PTC thermal performance.

2.2. EFFECT OF ADDING NANOPARTICLES TO THE HTF

Modified thermal properties of the new nanofluid can be calculated as follows:

2.2.1. Thermal conductivity

In the field of nanofluids, the Maxwell-Garnetts (MG) model is commonly used to describe how the thermal conductivity of a nanofluid (where particles are micrometers in size) changes as follows[64,65]:

$$K_{np} = K_{bf}\frac{K_p + 2K_{bf} - 2\phi(K_{bf} - K_p)}{K_p + 2K_{bf} + \phi(K_{bf} - K_p)} , \quad (25)$$

K_{np}, K_{bf}, and K_p are the thermal conductivities, measured in $W/m\,°K$, of nanofluid, base fluid and nanoparticles, respectively. And ϕ is the nanoparticles volume fraction. While for hybrid nanofluids case, thermal conductivity can be calculated as follows[40]:

$$K_{hf} = K_{bf}\frac{(\phi_1 K_1 + \phi_2 K_2)(1 + 2\phi_{hf}) + 2K_{bf}\phi_{hf}(1 - \phi_{hf})}{(\phi_1 K_1 + \phi_2 K_2)(1 - \phi_{hf}) + 2K_{bf}\phi_{hf}(1 - \phi_{hf})} , \quad (26)$$

where ϕ_1 and ϕ_2 represent volume fraction of the two mixed types of nanoparticles, such that $\phi_1 + \phi_2 = \phi_{hf}$. And K_1 and K_2 represent thermal conductivity of the two mixed types of nanoparticles.

2.2.2. Density

The applied nanofluid's effective density is defined by [66]:

$$\rho_{nf} = (1 - \phi)\rho_{bf} + \phi\rho_p, \quad (27)$$

where ρ_{nf}, ρ_p and ρ_{bf} represent densities, measured in kg/m^3 , of nanofluid, nanoparticles and base fluid, respectively. While for hybrid nanofluids case, density can be calculated as follows[40]:

$$\rho_{hf} = (1 - \phi_{hf})\rho_{bf} + \phi_1 \rho_1 + \phi_2 \rho_2 , \quad (28)$$

where ρ_1 and ρ_2 represent density of the two mixed types

of nanoparticles.

2.2.3. Specific heat

Nano fluid specific heat in $J/kg°K$ can be calculated as follows [67]:

$$c_{p-nf} = \frac{(1-\phi)(\rho c_p)_{bf} + \phi(\rho c_p)_p}{\rho_{nf}}, \qquad (29)$$

while for hybrid nanofluids case, specific heat can be calculated as follows[40]:

$$c_{p-hf} = \frac{(1-\phi_{hf})(\rho c_p)_{hf} + \phi_1(\rho c_p)_1 + \phi_2(\rho c_p)_2}{\rho_{hf}}, \qquad (30)$$

Gathering Eqs. (6), (16) and (17), we get the overall system 1-D model which represents coupled system of non-linear hyperbolic partial differential equations:

$$h_{con,f-abs}\pi\bar{d}_{abs}(T_{abs} - T_f) - \rho_f u_f A_{cf} c_{pf}\frac{\partial T_f}{\partial x} + k_f A_{cf}\frac{\partial^2 T_f}{\partial x^2} \qquad (31)$$
$$= \rho_f A_{cf} c_{pf}\left(\frac{\partial^\beta T_f}{\partial t^\beta} + \frac{\tau_f}{\Gamma(1+\alpha)}\frac{\partial^{1+\alpha}T_f}{\partial t^{1+\alpha}}\right), 0 < \beta < 1 \text{ and } 0 < \alpha < 1$$

$$I_{abs}(t)W - h_{f-abs}\pi\bar{d}_{abs}(T_{abs} - T_f) - h_{con,abs-r}\pi\bar{d}_{abs}(T_{abs} - T_r)$$
$$- h_{rad,abs-r}\pi\bar{d}_{abs}(T_{abs}^4 - T_r^4) + k_{abs}A_{c-abs}\frac{\partial^2 T_{abs}}{\partial x^2}$$
$$= \rho_{abs}A_{c-abs}c_{p-abs}\left(\frac{\partial^\beta T_{abs}}{\partial t^\beta} + \frac{\tau_{abs}}{\Gamma(1+\alpha)}\frac{\partial^{1+\alpha}T_{abs}}{\partial t^{1+\alpha}}\right), \qquad (32)$$

$$I_r(t)W + h_{con,abs-r}\pi\bar{d}_{abs}(T_{abs} - T_r)$$
$$+ h_{rad,abs-r}\pi\bar{d}_{abs}(T_{abs}^4 - T_r^4) - h_{con,r-atm}\pi\bar{d}_r(T_r - T_{atm})$$
$$- h_{rad,r-sky}\pi\bar{d}_r(T_r^4 - T_{sky}^4) + k_r A_{c-r}\frac{\partial^2 T_r}{\partial x^2}$$
$$= \rho_r A_{c-r}c_{p-r}\left(\frac{\partial^\beta T_r}{\partial t^\beta} + \frac{\tau_r}{\Gamma(1+\alpha)}\frac{\partial^{1+\alpha}T_r}{\partial t^{1+\alpha}}\right) \qquad (33)$$

where for $\beta \in (0,1)$ and according to [68],

$$\frac{\partial^\beta}{\partial t^\beta}T(x,t) = \frac{1}{\Gamma(1-\beta)}\int_0^t (t-\zeta)^{-\beta}\frac{\partial}{\partial\zeta}T(x,\zeta)d\zeta \qquad (34)$$

, and for $\alpha \in (0,1)$

$$\frac{\partial^{1+\alpha}}{\partial t^{1+\alpha}}T(x,t) = \frac{1}{\Gamma(1-\alpha)}\int_0^t (t-\zeta)^{-\alpha}\frac{\partial^2}{\partial\zeta^2}T(x,\zeta)d\zeta \qquad (35)$$

representing Caputo fractional derivative for unknown temperatures.
Subjected to initial conditions of:
$$T_f(x,0) = u(x), \quad T_{abs}(x,0) = v(x), \quad T_r(x,0) = w(x), \qquad (36)$$

which represents initial temperature distribution along the PTC length for HTF, absorber tube and glass receiver tube, respectively, at 9:00.
, and boundary conditions of:

$$\begin{cases} \frac{\partial T_r}{\partial x}(0,t) = 0, \qquad \frac{\partial T_r}{\partial x}(l,t) = 0, \\ \frac{\partial T_{abs}}{\partial x}(0,t) = 0, \qquad \frac{\partial T_{abs}}{\partial x}(l,t) = 0 \\ T_f(0,t) = Q_{in}(t), \quad \frac{\partial T_f}{\partial x}(l,t) = 0, \end{cases} \qquad (37)$$

where l is the total length of the absorber and receiver tube, $Q_{in}(t)$ represents fluid inlet temperature for entire calculation time from 9:00 to 17:00.

3. DISCRETIZATION

3.1. TEMPORAL DISCRETIZATION

According to [69], temporal fractional derivatives can be discretized as follows:

$$\frac{\partial^\beta}{\partial t^\beta}T(z,t) = \frac{1}{2\Gamma(1-\beta)\Delta t^\beta}\sum_{n=0}^{j-1}\omega_n^\beta(T_{j+1-n,i} - T_{j-1-n,i}) \qquad (38)$$

, and

$$\frac{\partial^{1+\alpha}}{\partial t^{1+\alpha}}T(z,t) = \frac{1}{\Gamma(1-\alpha)\Delta t^{1+\alpha}}\sum_{n=0}^{j-1}\omega_n^{1+\alpha}(T_{j+1-n,i} - 2T_{j-n,i} + T_{j-1-n,i}) \qquad (39)$$

where the weighting coefficients ω_n^β and $\omega_n^{1+\alpha}$ are defined as:

$$\omega_n^\beta = (n+1)^\beta - n^\beta \qquad (40)$$

, and

$$\omega_n^{1+\alpha} = (n+1)^{1+\alpha} - n^{1+\alpha} \qquad (41)$$

where the indices i and j stands for spatial and temporal grid points respectively,

3.2. SPATIAL DISCRETIZATION

Spatial integer order derivatives can be discretized by using central difference approximation as follows:

$$\left(\frac{\partial T}{\partial x}\right)_{j,i} = \frac{T_{j,i+1} - T_{j,i-1}}{2\Delta x}, \qquad \left(\frac{\partial^2 T}{\partial x^2}\right)_{j,i} = \frac{T_{j,i+1} - 2T_{j,i} + T_{j,i-1}}{\Delta x^2}, \qquad (42)$$

By placing Eqs. (38), (39) and (42) into Eqs. (31), (32) and (33) yields the following system of difference equations:

$$h_{con,f-abs}\pi\bar{d}_{abs}(T_{abs,j,i} - T_{f,j,i}) - \rho_f u_f A_{cf} c_{pf}\frac{T_{f,j,i+1} - T_{f,j,i-1}}{2\Delta x} + k_f A_{cf}\frac{T_{f,j,i+1} - 2T_{f,j,i} + T_{f,j,i-1}}{\Delta x^2} =$$
$$\rho_f A_{cf} c_{pf}\left(\frac{1}{2\Gamma(1-\beta)\Delta t^\beta}\sum_{n=0}^{j-1}\omega_n^\beta(T_{f,j+1-n,i} - T_{f,j-1-n,i}) + \right.$$
$$\left. \tau_f \frac{1}{\Gamma(1-\alpha)\Delta t^{1+\alpha}}\sum_{n=0}^{j-1}\omega_n^{1+\alpha}(T_{f,j+1-n,i} - 2T_{f,j-n,i} + T_{f,j-1-n,i})\right), \qquad (43)$$

$$I_{abs,j}W - h_{con,f-abs}\pi\bar{d}_{abs}(T_{abs,j,i} - T_{f,j,i}) - h_{con,abs-r}\pi\bar{d}_{abs}(T_{abs,j,i} - T_{r,j,i}) -$$
$$h_{rad,abs-r}\pi\bar{d}_{abs}(T_{abs,j,i}^4 - T_{r,j,i}^4) + k_{abs}A_{c-abs}\frac{T_{abs,j,i+1} - 2T_{abs,j,i} + T_{abs,j,i-1}}{\Delta x^2} =$$
$$\rho_{abs}A_{c-abs}c_{p-abs}\left(\frac{1}{2\Gamma(1-\beta)\Delta t^\beta}\sum_{n=0}^{j-1}\omega_n^\beta(T_{abs,j+1-n,i} - T_{abs,j-1-n,i}) + \right.$$
$$\left. \tau_{abs}\frac{1}{\Gamma(1-\alpha)\Delta t^{1+\alpha}}\sum_{n=0}^{j-1}\omega_n^{1+\alpha}(T_{abs,j+1-n,i} - 2T_{abs,j-n,i} + T_{abs,j-1-n,i})\right) \qquad (44)$$

$$I_{r,j}W + h_{con,abs-r}\pi\bar{d}_{abs}(T_{abs,j,i} - T_{r,j,i}) + h_{rad,abs-r}\pi\bar{d}_{abs}(T_{abs,j,i}^4 -$$
$$T_{r,j,i}^4) - h_{con,r-atm}\pi\bar{d}_r(T_{r,j,i} - T_{atm,j}) - h_{rad,r-sky}\pi\bar{d}_r(T_{r,j,i}^4 - T_{sky,j}^4) +$$
$$k_r A_{c-r}\frac{T_{r,j,i+1} - 2T_{r,j,i} + T_{r,j,i-1}}{\Delta x^2} = \rho_r A_{c-r}c_{p-r}\left(\frac{1}{2\Gamma(1-\beta)\Delta t^\beta}\sum_{n=0}^{j-1}\omega_n^\beta(T_{r,j+1-n,i} - T_{r,j-1-n,i}) + \right.$$
$$\left. \tau_r \frac{1}{\Gamma(1-\alpha)\Delta t^{1+\alpha}}\sum_{n=0}^{j-1}\omega_n^{1+\alpha}(T_{r,j+1-n,i} - 2T_{r,j-n,i} + T_{r,j-1-n,i})\right) \qquad (45)$$

Dividing all three solution meshes into "m" number of rows and "n" number of columns, where $N = (m-2)*(n-2)$ which represents number of unknowns for each mesh after assuming suitable initial and boundary conditions. The solution of the coupled system can be solved using MATLAB implicitly by applying Newton-Raphson formula by choosing meshes steps to be $\Delta t = 0.001\ hr$ and $\Delta x = 0.01\ m$ for solution stability and mesh grid independence. It's worth noting that Eqs. (43), (44) and (45) would represent classical Fourier model if relaxation time "τ" equals to zero, and $\beta \rightarrow 1$.

4. RESULTS AND DISCUSSION

4.1. VALIDATION OF THE PROPOSED FRACTIONAL SPL MODEL

Fig. 4 shows hourly-varying weather conditions measured during daytime including solar radiation intensity, ambient temperature, and wind speed by Hamada et al. [55] on Aug. 1st, 2021 , the figure demonstrate a progressive increase in solar radiation intensity from starting the measurements at 9:00 till it reaches its maximum value of $917\ W/m^2$ at 13:00, then it declines gradually till the end of the measuring time at 17:00.

First, the new proposed model will be solved by choosing different values of $\tau, \alpha,$ and β in the acceptable range. Then, obtained results will be compared with those obtained experimentally by Hamada et al. [55] on Aug. 1st, 2021.

Calculated results show that altering fractional order, β, for fractional Fourier model (i.e. no time phase lag is considered), affects significantly calculated temperatures, where water outlet temperatures increase gradually by decreasing the value of β as shown in Fig. 5 (a) and (b). on the other hand, adding relaxation time, τ, to Fourier model doesn't affect results significantly, where curves almost coincide with ones obtained by solving the integer-order Fourier model. However, for $\beta = 1$, and for any small relaxation time ($\tau \leq 1 \times 10^{-3}$ hours), altering the fractional order value of α, associated with time phase lag part, cause a slight shifting for temperature curves, where decreasing α values decrease marginally water outlet temperatures, causing a little shifting for temperature curves downwards as shown in Fig. 5 (a) and (b).

In order to determine thermal delay times and fractional orders achieving best experimental-matching results, we used a grid search optimization technique. This method aimed to minimize the squared difference error between the experimental results and the model's predictions by using the following objective function:

$$min\frac{\sqrt{\sum_{j=1}^{n-2}\left(T_{f,j} - T_{exp,j}\right)^2}}{\sqrt{\sum_{j=1}^{n-2}\left(T_{exp,j}\right)^2}} \qquad (46)$$

where in the equation, $T_{exp,j}$ and $T_{f,j}$ denote the experimental and model-predicted water temperatures,

respectively, at each specific time point j. The grid search optimization explored a range of possible values for the fractional order parameters α and β. Both α and β are constrained to lie within the interval $(0,1)$. Calculated results presented in Fig. 5 (c) shows that optimum solution obtained was for the case of fractional Fourier model, where $\beta = 0.8$, and $\tau = 0$, at which calculated error obtained from mentioned objective function (46) was 0.015937 compared with the value 0.015943 obtained from the case of integer-order Fourier model. It's worth noting that for the optimum case at which $\beta = 0.8$, which will be used for all preceding calculations in the study, calculated average water outlet temperature was $50.872\ °C$ compared with an average value of $50.885\ °C$ obtained from experimental results.
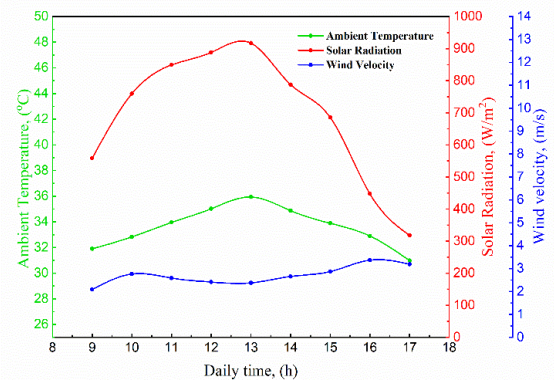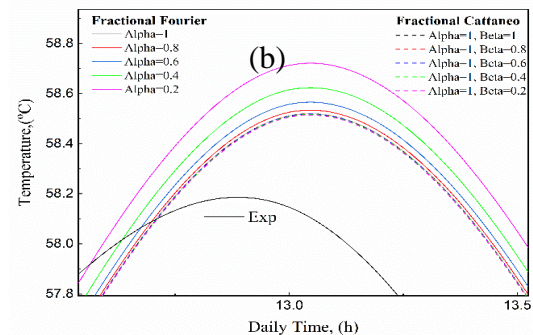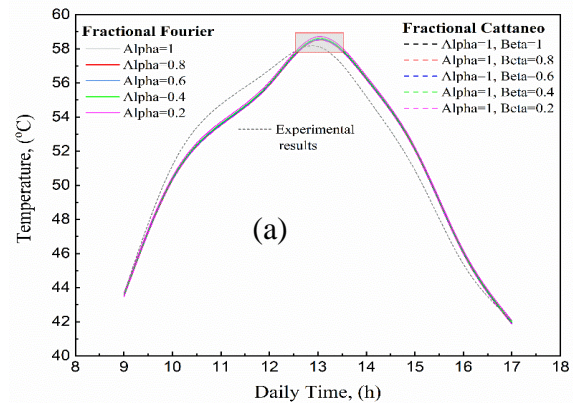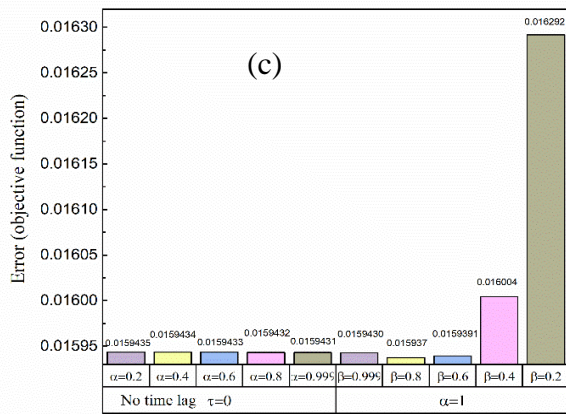

Fig. 4. Hourly-varying weather conditions for reference day

Fig. 5. (a) Hourly variating water outlet temperature at various time fractional orders, (b) Enlarged view for the rectangular selected area, (c) Error calculated by predefined error objective function

4.2. EFFECT OF ADDING NANOPARTICLES INTO HTF

Inserting several types of nanomaterials including CuO, TiO2 and Al2O3 into the HTF, water, with different concentrations and at a constant water flow rate of 20L/h will be discussed. Table 3 shows the thermophysical properties of the introduced nanoparticles.

Fig. 6 shows the result of comparing water outlet temperature and daily thermal efficiencies for using the mentioned three types of nanofluids by a volume concentration value of 1%, results show that maximum calculated water temperature was 59.2 °C for the case of CuO nanofluid, followed by a temperature value of 58.73 °C and 58.62 °C for the case of using TiO2 and Al2O3 nanofluids respectively, therefore, maximum percentage increment in water temperature was for the case of adding CuO nanoparticles to flowing water with a maximum value of 1.18 %, also daily average thermal efficiency was enhanced by 5.28 %.

Fig. 7 shows the effect of altering the volume concentration value of CuO nanoparticles, which lead to the best performance among the three mentioned types, results show that decreasing CuO nanoparticles concentration percentage decreases both water outlet temperature and thermal efficiency.

Fig. 8 (a), (b) and (c), compare the thermophysical properties of water after mixing it with hybrid nanoparticles with total concentration of 1%. Three mixtures of hybrid nanofluids were discussed including CuO- TiO2, CuO- Al2O3, and TiO2- Al2O3 nanofluids, where for Fig. 8 (a) and (b),

increasing CuO nanoparticles concentration gradually while maintaining total nanoparticles concentration at 1%, increases both nanofluid thermal conductivity and density while reduces its specific heat.

Fig. 8 (c) shows that increasing TiO2 nanoparticles concentration gradually reduces both fluid thermal conductivity and density while increases its specific heat. Fig. 9 shows the effect of incorporating CuO-TiO2 nanofluid as a HTF for the discussed conventional PTC, this mixture was chosen as it holds the best thermophysical properties among the three mentioned mixtures, results show that by keeping total nanoparticles concentration at 1% and increasing CuO nanoparticles concentration gradually, HTF outlet temperature and thermal efficiency was increased till they reached their maximum values at total CuO nanoparticles concentration with no TiO2 nanoparticles ingredient, and that can be justified by Fig. 8 (c) which shows that increasing CuO nanoparticles concentration while keeping total concentration at constant value, increases nanofluid thermal conductivity and reduces its heat capacity.
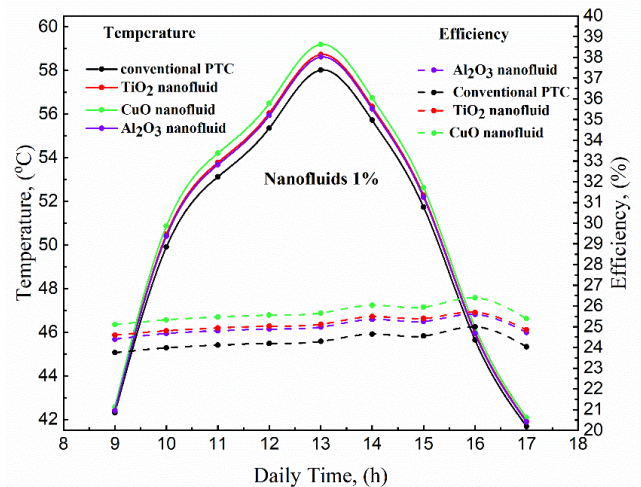

Fig. 6. Water outlet temperature and thermal efficiency for CuO, TiO2 and Al2O3 nanofluids for 1% volume concentration
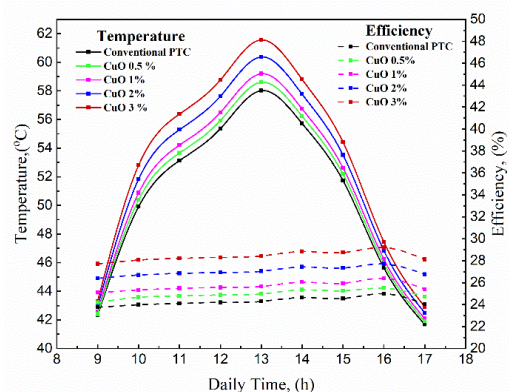

Fig. 7. Water outlet temperature and thermal efficiency for

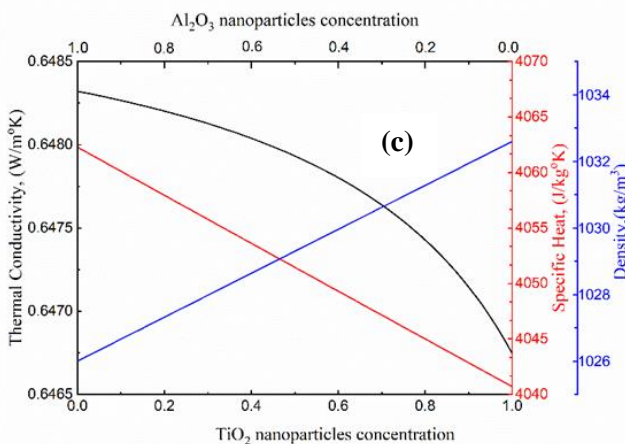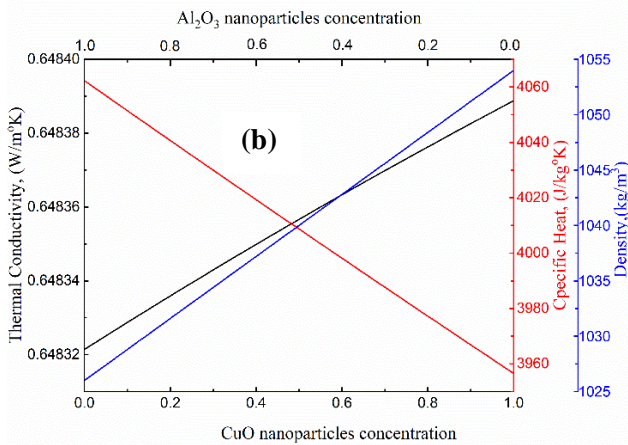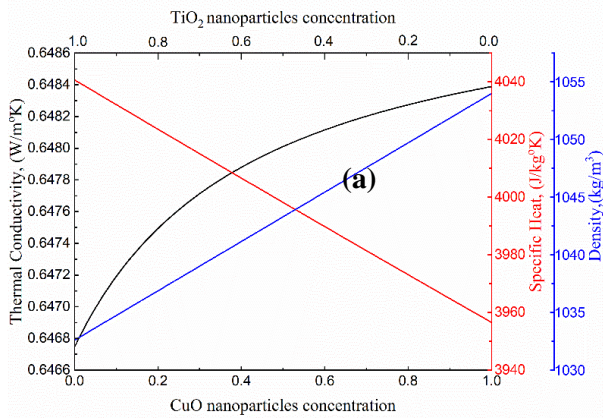*CuO nanofluid at different volume concentrations.*

Fig. 8. Thermophysical properties of (a) CuO-TiO₂ hybrid nanofluid, (b) CuO-Al₂O₃ hybrid nanofluid , (c) TiO₂- Al₂O₃ hybrid nanofluid, at different concentrations.
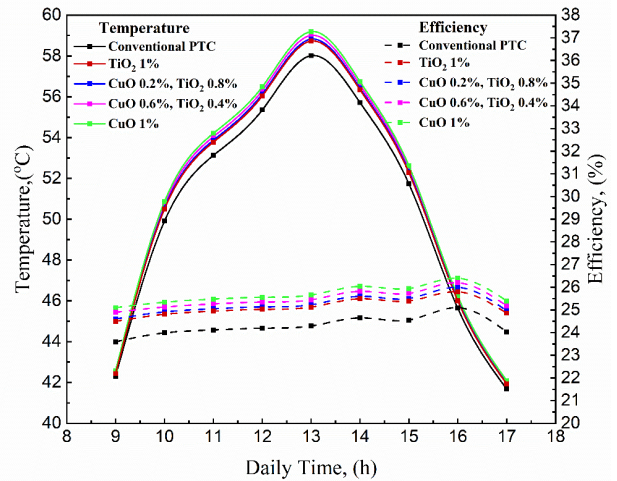

Fig. 9. Outlet water temperature and thermal efficiency for CuO-TiO₂ hybrid nanofluid at different volume concentrations.

Table 3. Thermophysical properties of employed nanoparticles [40,55]

Nanomaterial type	Density (kg/m³)	Specific heat capacity (J/kg K)	Thermal conductivity (W/m K)
Al₂O₃	3600	880	30
CuO	6000	551	33
TiO₂	4260	850	9

4.3.   EFFECT OF ADDING NANOCOATING

Coating PTC absorber with black paint enhances significantly PTC thermal performance, owning to black paint high solar absorptance. Despite of the large value of black paint solar absorptance, this value can be enhanced by inserting nanoparticles with superior thermal properties to black paint used. Abdelkader et al. [70] studied experimentally solar absorptance and thermal emittance of black paint mixed with several concentrations of carbon nanotubes (CNTs) and an equal mixture of CNTs and CuO. Properties of CuO and CNTs used by Abdelkader et al. are mentioned in Table 4, while solar absorptance and thermal emittance of these materials are mentioned in Table 5. Several mass concentrations of black paint mixed with mentioned nanoparticles will be used as coating for PTC absorber made of copper holding water as the HTF.

Fig. 10 (a) shows that increasing mass concentration of CNTs increases both water outlet temperature and thermal efficiency, reaching the maximum values for the case of using CNTs of mass concentration of 5% at which average temperature

difference reaches 21.7 °C and average efficiency reaches 33.67%. Fig. 10 (b) shows the results of mixing CuO nanoparticles with equal amounts of CNTs to be dispersed in the black paint to be used as coating for the absorber tube. Temperature difference and thermal efficiency for nanoparticles mixture of mass concentrations of 1%, 3%, and 5% were calculated. Average temperature difference was 21.32 °C, 21.42 °C, and 21.44 °C, respectively, while average thermal efficiency was 33.08%, 33.24%, and 33.27%, respectively.

Table 4. Properties of implied CNTs and CuO nanoparticles [70]

Name	Nanometer CuO	Industrial CNTs
Color	Black powder	Black powder
Purity	99.5$wt\%$	95%
Inner diameter	−	$3-5\ nm$
Outer diameter	$40\pm5nm$	$8-15\ nm$
length	−	$3-12\ nm$

Table 5. Solar absorptance (γ) and thermal emittance (ε) for different mass concentration of CNTs-black paint and CNT/CuO-black paint [70].

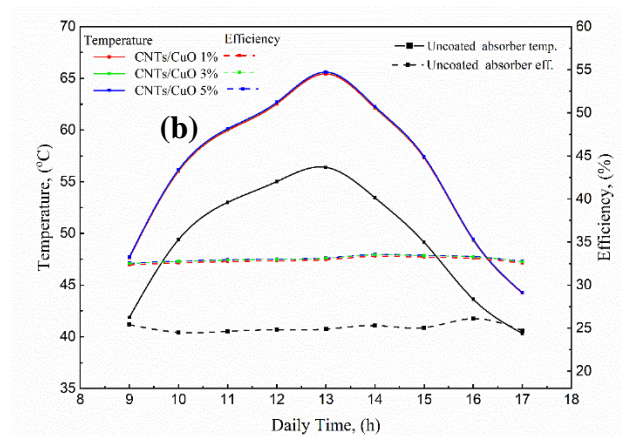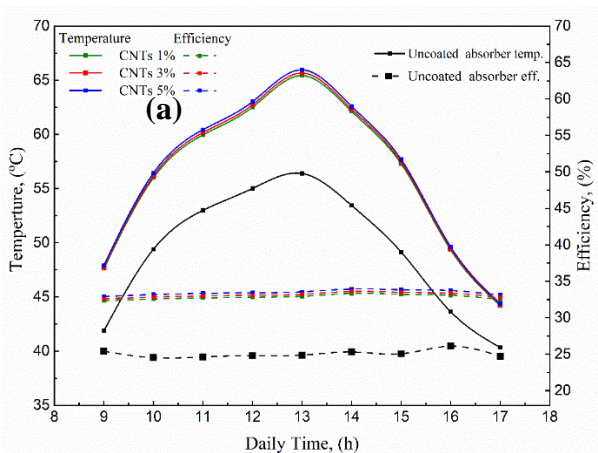| Sample	γ	ε	Sample	γ	ε
Black paint	0.954	0.157	CuO+CNTs 1%	0.958	0.132
CNTs 1%	0.959	0.169	CuO+CNTs 3%	0.963	0.137
CNTs 3%	0.967	0.171	CuO+CNTs 5%	0.965	0.165
CNTs 5%	0.979	0.224	−	−	−

Fig. 10. Water outlet temperature and thermal efficiency for the case of using different mass concentrations for (a) CNTs nano-coating, (b)hybrid CNTs and CuO nano-coating.

5. Conclusion

This paper presents a novel fractional modeling approach for U-type parabolic trough collectors that incorporates Cattaneo heat flux to account for thermal wave effects. First, the new model was examined for various relaxation times and fractional orders, in order to achieve best matching results with experimental data. Then, optimum chosen case was used for improving PTC thermal performance by incorporating different nanomaterials, obtained results can be summarized as follows:

Altering fractional order, β, for fractional Fourier model (i.e. no time phase lag is considered), affects significantly calculated temperatures, where water outlet temperatures increase gradually by decreasing the value of β.

Adding relaxation time, τ, to Fourier model doesn't affect results significantly, where curves almost coincide with ones obtained by solving the integer-order Fourier model.

For $\beta = 1$, and for any small relaxation time ($\tau \leq 1 \times 10^{-3}$ hours), altering the fractional order value of α, associated with time phase lag part, cause a slight shifting for temperature curves, where decreasing α values decrease marginally water outlet temperatures, causing a little shifting for temperature curves downwards.

Optimum solution obtained was for the case of fractional Fourier model, where $\beta = 0.8$, and $\tau = 0$, at which calculated average water outlet temperature was $50.872\ °C$ compared with an average value of $50.885\ °C$ obtained from experimental results.

Several nanoparticles including CuO, TiO_2 and Al_2O_3 added to water at different volume concentrations were discussed.

Thermophysical properties for various hybrid nanofluids, including $CuO-TiO_2$, $CuO-Al_2O_3$, and $TiO_2-Al_2O_3$ nanofluids were discussed, while $CuO-TiO_2$ nanofluid was chosen as the PTC's HTF to study its performance, because it holds the best thermophysical properties among the mentioned nanofluids.

Best results obtained were for the case of adding 3% volume concentration of CuO nanoparticles, at which average outlet fluid temperature and thermal efficiency was 52.93 °C and 28.4% compared with 50.1 °C and 24.25% for the conventional case where no nanoparticles are added.

The effect of Reynolds number on convection heat transfer coefficient and pressure drop across tube inlet and outlet were discussed for different nanofluids at different concentrations, where maximum pressure drop occurs for the case of Al_2O_3 nanofluid (1% concentration), while the highest achieved heat transfer coefficient was for the case of CuO nanofluid.

Coating PTC absorber with black paint mixed with nanoparticles enhances significantly PTC thermal performance, where two types of nanoparticles were used, CNTs and CuO individually and in mixture.

Increasing mass concentration of CNTs increases both water outlet temperature and thermal efficiency, reaching the maximum values for the case of using CNTs of mass concentration of 5% at which average temperature difference reaches 21.7 °C and average efficiency reaches 33.67%.

Mixing CuO nanoparticles with equal amounts of CNTs at different mass concentrations of 1%, 3%, and 5% were discussed, where average temperature difference between water outlet and inlet was 21.32 °C, 21.42 °C, and 21.44 °C, respectively.

APPENDIX

Table 6. thermophysical properties for different PTC components used in the study [59,71]

Variable	Quantity
Transmittance of the evacuated tube	0.96
Absorptance of the evacuated tube	0.04
Emittance of the evacuated tube	0.9
Density of the Evacuated tube	2700 kg/m³
Specific heat of the evacuated tube	790 J/kg K
Thermal conductivity of the evacuated tube	0.9 W/m K
Absorptivity of copper material	0.76
Emittance of copper material	0.02
Density of copper material	8900 kg/m³
Specific heat of copper material	390 J/kg K
Thermal conductivity of copper material	400 W/m K

Thermophysical properties of Water:

$$\rho_w = \sum_{n=1}^{5} a_n T_w^{n-1} \times \sum_{n=1}^{5} b_n T_w^{n-1}$$

$a_1 = 9.9 \times 10^2$
$a_2 = 2.1 \times 10^{-2}$
$a_3 = -6.2 \times 10^{-3}$
$a_4 = 2.3 \times 10^{-5}$
$a_5 = -4.6 \times 10^{-8}$
$b_1 = 8.1 \times 10^2$
$b_2 = -2$
$b_3 = 1.7 \times 10^{-2}$
$b_4 = -3 \times 10^{-5}$
$b_5 = 1.7 \times 10^{-5}$

where T_w (°C) represents inlet water temperature, a_n and b_n (kg/m³.(°C)^{n-1}) are constants

$C_w = \left(A + BT_{W,K}, + CT_{W,K}^2 + DT_{W,K}^3\right) \times 10^3$

$A = 0.4 \times 10^{-3}S^2 - 0.098S + 5.3 \left(\frac{J}{kg.K}\right)$

$B = -320 \times 10^{-4}S^2 + 740 \times 10^{-6}S - 690 \times 10^{-5}\left(\frac{J}{kg.K^2}\right)$

$C = 820 \times 10^{-11}S^2 - 190 \times 10^{-8}S + 0.9 \times 10^{-5} \left(\frac{J}{kg.K^3}\right)$

$D = -70 \times 10^{-13}S^2 + 170 \times 10^{-11}S + 20 \times 10^{-10} \left(\frac{J}{kg.K^4}\right)$

where salinities (S) are available from $(0 - 150)$ $\frac{g}{kg}$.

Thermophysical properties of Syltherm 800:

$\rho = 1.1057 \times 10^3 - 0.41535T - 6.0616 \times 10^{-4}T^2 \ (kg/m^3)$

$\mu = +8.4866 \times 10^{-2} - 5.5412 \times 10^{-4}T + 1.3882 \times 10^{-6}T^2 - 1.566 \times 10^{-9}T^3 + 6.672 \times 10^{-13}T^4 \ (Pa.s)$

$k = 0.19002 - 1.875 \times 10^{-4}T - 5.7534 \times 10^{-10}T^2 , (W/m.K)$

$C_p = 1.1078 \times 10^3 + 1.708T , (J/kg.K)$

Where T is in Kelvin.

Thermophysical properties of Therminol R66:

$\rho = -0.61425(T - 273) - 0.34 \times 10^{-3}(T - 273)^2 + 1020.62 \left(\frac{kg}{m^3}\right),$

$$C_p = 0.003313 \ (T - 273) - 8.971 \times 10^{-7}(T - 273)^2$$
$$+ \ 1.496 \ \left(\frac{KJ}{kg.K}\right),$$
$$k = -0.33 \times 10^{-4}(T - 273) - 0.15 \times 10^{-6}(T - 273)^2$$
$$+ \ 0.11829 \ \left(\frac{W}{m.K}\right),$$
$$\nu = e^{\left(\frac{586.375}{(T-273)+62.5} - 2.2809\right)} \ \left(\frac{mm^2}{s}\right)$$

Where T is in Kelvin.

REFERENCES

[1] Goethert, B., "Noise Attenuation and Associated Thrust Increase of Turbojet Engine through Hyper-Mixing Ejector Shrouds", 5th International Symposium on Air Breathing Engine, ISABE 81, India, pp. 17.1-17.11, 1981.

[2] O'Sullivan, M.N., "A Computational Study of Viscous Effects on Lobed Mixer Flow Features and Performance", manuscript in preparation, 1993.

[3] Keenan, J.H., and Neumann, E.P., "A Simple Air Ejector", Journal of Applied Mechanics, 9, A75-AS1, 1942.

[4] Von Karman, T., "Theoretical Remarks on Thrust Augmentation", In Contributions to Applied Mechanics (Reissner AnniversaryVolume), pp. 461-468, 1949.

[5] Quinn, B., " Thrust Augmenting Ejectors", A Review of the Application of Jet Mechanics to V/STOL Aircraft Propulsion, AGARD CPP-308, 19.1-19.14, 1981.

[6] Porter, J.L., Sqnyers, R.A., and Nagaraja, K.S., "An Overview of Ejector Theory", AIAA Paper No. 81-1678, 1981.

[7] Bevilaqua, P.M., "Advances in Ejector Thrust Augmentation", In Recent Advances in Aerodynamics, Springer-Verlag, New York, pp. 375-405, 1985.

[8] Alperin, M. and Wu, J. J., "Thrust Augmenting Ejectors, Part I" AIAA Journal, Vol. 21, No. 10, October 1983, pp. 1428-1436.

[9] Alperin, M. and Wu, J. J., "Thrust Augmenting Ejectors, Part II" AIAA Journal, Vol. 21, No. 12, , pp. 1428-1436, December 1983.

[10] Bevilaqua, P.M., "Lifting Surface Theory for Thrust Augmenting Ejectors" AIAA Journal, Vol. 16, No. 5, May 1978, pp. 475-481.

[11] Fisher, S.A. and Irvine, R.D., "Air Augmentation of Rocket for Low Speed Application," 5th ISABE 81, INDIA, pp.26.1-26.8. 1981.

[12] EL-Banna, R.A.M, "New Concepts in Thrust Augmentor Ejectors", SECOND A.S.A.T. Conference, Cairo-Egypt, 21-23 April 1987.

[13] Whitley, N., Krothapalli, A. and Van Dommelen, L. "A Determinate Model of Thrust-Augmenting Ejectors", Theoretical and Computational Fluid Dynamics, 8:37-55, 1996.

[14] Raman, G. and Taghavi, R., "Aeroacoustic Characteristics of a Rectangular Multi-Element Supersonic Jet Mixer-Ejector Nozzle", Journal of Sound and Vibration 207(2), 227-247, 1997.

[15] Okai, K., Taguchi, H. and Futamura, H., "Experimental and Numerical Investigations of Ejector and Mixing Effects in a Model Ejector Ramjet Configuration", ISABE 2003-1230.

[16] Aissa, W.A., "Effect of Throat Length on the Performance of an Air Ejector", ISABE 2003-1121.

[17] Aissa, W.A., "Experimental and Analytical Investigation of an Air Jet Ejector", Mansoura 4th International Engineering Conference, Sharm El-Shiekh, Egypt, pp. 171-176, April 20-22, 2004.

[18] A.E. Kabeel, A.M. El-Zahaby, E.A. El-Shenawy, A.I. Bakry, Z.M. Omara. The infrared suppression and cooling by utilizing ejectors. Contemporary Technology and Applied Engineering (JCTAE), 1(1), 2022, 82-88. DOI: 10.21608/JCTAE.2022.160264.1010.

[19] Schmidt R., A Hupfer. Design and numerical simulation of ejector nozzles for very small turbojet engines. CEAS Aeronautical Journal 2021. https://doi.org/10.1007/s13272-021-00537-3.

[20] A. Hupfer, Hirndorf, D. Investigation of parameters affecting thermodynamic cycle of very small jet engines. In: Proceedings of 15th International Symposium on Transport Phenomena and Dynamics of Rotating Machinery (ISROMAC-15), Honolulu (2014)

[21] Patankar, S. V., "Numerical Heat Transfer and Fluid Flow", Hemisphere Publishing Company, New York, 1980.

[22] Launder, B. E. and Spalding, D. B., "The Numerical Computation of Turbulent Flows", Computer Methods in Applied Mechanics and Engineering, 3:269-289, 1974.

[23] Binder, G. and Didelle, H., "Improvement of Ejector Thrust Augmentation by Pulsating or Flapping Jets", published by BHRA Fluid Engineering, Cranfield, Bedford, England. March,1985.

[24] Carletti, M., Rogers, C.B. and Parekh, D.E., "Use of Streamwise Vorticity to Increase Mass Entrainment in a Cylindrical Ejector", AIAA Journal, Vol. 33, No. 9, pp. 1641-1645, Sept. 1995.